10-20-2002

Production, Outflow, Velocity, and Radial Distribution of H2O and OH in the Coma of Comet C/1995 O1 (Hale-Bopp) from Wide-field Imaging of OH

Walter M. Harris
University of Wisconsin-Madison

Frank Scherb
University of Wisconsin-Madison

Edwin Mierkiewicz
University of Wisconsin - Madison, mierkiee@erau.edu

Ronald Oliversen
Goddard Space Flight Center

Jeffrey Morgenthaler
University of Wisconsin-Madison

The Astrophysical Journal, 578:996–1008, 2002 October 20

PRODUCTION, OUTFLOW VELOCITY, AND RADIAL DISTRIBUTION OF H_2O AND OH IN THE COMA OF COMET C/1995 O1 (HALE-BOPP) FROM WIDE-FIELD IMAGING OF OH

Walter M. Harris,[1] Frank Scherb,[1] Edwin Mierkiewicz,[1] Ronald Oliversen,[2] and Jeffrey Morgenthaler[1]

Received 2001 October 19; accepted 2002 June 24

ABSTRACT

Observations of OH are a useful proxy of the water production rate (Q_{H_2O}) and outflow velocity (V_{H_2O}) in comets. From wide-field images taken on 1997 March 28 and April 8 that capture the entire scale length of the OH coma of comet C/1995 O1 (Hale-Bopp), we obtain Q_{OH} from the model-independent method of aperture summation and Q_{H_2O} from the OH photochemical branching ratio, BR_{OH}. Using an adaptive ring summation algorithm, we extract the radial brightness distribution of OH 0–0 band emission out to cometocentric distances of up to 10^6 km, both as azimuthal averages and in quadrants covering different position angles relative to the comet–Sun line. These profiles are fitted using both fixed and variable velocity two-component spherical expansion models to estimate V_{OH} with increasing distance from the nucleus. The OH coma of Hale-Bopp was more spatially extended than those of previous comets, and this extension is best matched by a variable acceleration of H_2O and OH that acted across the entire coma, but was strongest within 1–2×10^4 km from the nucleus. Our models indicate that V_{OH} at the edge of our detectable field of view (10^6 km) was ~2–3 times greater in Hale-Bopp than for a 1P/Halley class comet at 1 AU, which is consistent with the results of more sophisticated gas-kinetic models, extrapolation from previous observations of OH in comets with $Q_{H_2O} > 10^{29}$ s^{-1}, and direct radio measurements of the outer coma Hale-Bopp OH velocity. The likely source of this acceleration is thermalization of the excess energy of dissociation of H_2O and OH over an extended collisional coma. When the coma is broken down by quadrants in position angle, we find an azimuthal asymmetry in the radial distribution that is characterized by an increase in the spatial extent of OH in the region between the orbit-trailing and anti-Sunward directions. Model fits specific to this area and comparison with radio OH measurements suggest greater acceleration here, with $V_{OH} \sim 1.5$ times greater at a 10^6 km cometocentric distance than elsewhere in the coma. We discuss several mechanisms that may have acted within the coma to produce the observed effect.

Subject heading: comets: individual (Hale-Bopp 1995 O1)

1. INTRODUCTION

The study of conditions in comet comae must necessarily begin with an understanding of water. As the dominant volatile component liberated from comet nuclei, the production rate, source geometry, temperature, outflow characteristics, solar wind interaction, and photochemical evolution of water sets the stage for much of the activity in the coma. Water has no visible or UV emission lines and is thus difficult to measure directly. Direct observations of cometary water are now performed over small fields of view in the IR (Dello Russo et al. 2000); however, the most effective methods for deriving the characteristics of water over the entire coma have historically been from studies of its daughter products, H, O, and OH. The distribution and/or brightness of each daughter species can be used to derive water production, provided specific knowledge of an appropriate set of physical characteristics (e.g., formation rate, lifetime, outflow velocity, radial distribution, etc.) is available. These ancillary parameters will vary depending on the daughter species studied and are known to differing degrees of accuracy that depend on the solar radiation field, heliocentric velocity, and the total gas production from the comet. The interpretation of water production and evolution from a single measurement or species will therefore vary with the degree of uncertainty in the underlying assumptions (Schleicher, Mills, & Birch 1998). Fortunately, the different aspects of water production are complementary, and greatly improved convergence is obtained from coordinated observations (Combi et al. 2000).

This paper contains a detailed examination of the production rate, radial distribution, and velocity structure of OH in C/1995 O1 (Hale-Bopp) from wide-field images taken during a 2 week period bracketing its perihelion passage. Hale-Bopp was a unique object in the modern astronomical era, one that provided our best opportunity to date to study the physical properties of water production and evolution, and the effects of collisional processes in the coma at the extreme high end of comet gas production. Because of Hale-Bopp's very high activity, the OH emissions were bright enough for us to overcome several magnitudes of atmospheric attenuation, allowing us to detect them out to cometocentric distances greater than 10^6 km. Over this field of view (FOV), we imaged the entire photochemical scale length of OH, and could thus derive Q_{H_2O} using only the $H_2O \rightarrow OH$ branching ratio. To determine the first-order velocity structure of the coma as an azimuthal average and over position angle (P.A.) sectors relative to the comet–Sun line, we fitted the radial profiles with two types of spherical expansion models. The model fits show evidence of acceleration over most of the coma that breaks down in regions characterized by a strong velocity gradient within a few $\times 10^4$ km of the nucleus and a slower process acting over greater distances. These results compare favorably with conclusions derived from more detailed gas-kinetic models (Combi et al. 1999) and other complementary observations

[1] University of Wisconsin–Madison, 1150 University Avenue, Madison, WI 53706.
[2] Goddard Space Flight Center.

TABLE 1
OH OBSERVATIONS OF HALE-BOPP AT THE BURRELL SCHMIDT

Observation Date	Observation Time	r[a] (AU)	Δ[b] (Au)	P.A.$_R$[c] (deg)	P.A.$_V$[d] (deg)	FOV (km)	Air Mass	Q_{H_2O}[e] (10^{30} s^{-1})
1997 Mar 28...	02:31:58	0.917	1.327	15.6	285	4.646×10^6	2.98–3.22	9.31 ± 1.4
1997 Apr 08....	02:52:14	0.920	1.418	39.8	308	4.965×10^6	2.55–2.74	10.8 ± 1.6

[a] Heliocentric distance.
[b] Geocentric distance.
[c] Position angle of the Sun–comet extended radius vector.
[d] Position angle of the comet velocity vector.
[e] Production rate derived from aperture summation.

of OH (Colom et al. 1999; Woods, Feldman, & Rottman 2000) and other coma volatiles (Biver et al. 1999). We also report on the presence of an extended OH radial distribution in the trailing sectors of the coma that has also been seen in observations of metastable O(^1D) (Morgenthaler et al. 2001) and we provide a discussion of some possible mechanisms that could produce it.

2. TECHNIQUES FOR USING OH AS A PROXY FOR Q_{H_2O} AND $V_{OH}(r)$

OH is a good candidate for deriving Q_{H_2O} and the other dynamical properties of the coma. It has only one significant formation pathway (H_2O), whereas the other water byproducts, O and H, may be both chemical daughters *and* granddaughters of H_2O, in addition to having multiple parents (in particular, O may come in significant quantities from CO and CO_2). The O and H emissions have other complicating characteristics, such as collisional quenching of the visible O(^1D) transition (Schultz et al. 1993) and hydrogen's complex velocity structure (Smyth et al. 1993), large scale length, and interactions with the solar wind and solar radiation field. About ~90% of OH is formed directly from H_2O into the $X\,^2\Pi$ ground state (Budzien, Festou, & Feldman 1994; Van Dishoeck & Dalgarno 1984), which results in a bright, high-contrast resonance fluorescence emission that is accessible from ground-based telescopes. The OH scale length against photodestruction is much shorter than for O or H (Huebner, Keady, & Lyon 1992), and it can thus be imaged in its entirety with an intermediate- to large-FOV telescope.

The OH life cycle follows three primary steps, beginning with the photodestruction of H_2O, followed by a radial expansion away from the nucleus, and ending with its dissociation or ionization. This chemical pathway ($H_2O \rightarrow OH \rightarrow O + H, OH^+$) has been studied extensively both theoretically and observationally (Budzien et al. 1994; Schleicher & A'Hearn 1988; Van Dishoeck & Dalgarno 1984), and, while recent observations of O(^1D) suggest that the dissociation branching ratios of OH to its daughters may need to be reviewed (Morgenthaler et al. 2001), the overall lifetime, state structure, and fluorescence efficiency of OH appear to be relatively well understood as functions of solar flux and heliocentric velocity. Because these various parameters all contain information about the evolution of water in the coma, to the extent that they are known, it is possible to invert the OH distribution to a map of water production either by fitting outflow models to the observed radial distribution or by adding all of the photons from the OH coma.

2.1. Q_{H_2O} *from Aperture Summation*

If the angular extent of the coma is smaller than a telescope FOV, and the signal level of OH is great enough to overcome atmospheric extinction, one can sum all the photons in the FOV and determine Q_{OH} (and thus Q_{H_2O}) with knowledge of only the g-factor, the lifetime against OH photodissociation, and the branching ratio from H_2O. With this technique, Q_{H_2O} is derived from

$$Q_{OH} = N_{OH}\Omega\Delta^2/\tau_{OH}\ , \tag{1}$$

where Ω is the solid angle of the FOV in radians, Δ is the geocentric distance (cm), τ_{OH} is the photochemical lifetime of OH in seconds, and N_{OH} is the average column density (cm^{-2}) over the field of view. The column density comes from the total signal in the aperture,

$$N_{OH} = 10^6 I_{OH}/g\ , \tag{2}$$

where I_{OH} is the field-averaged brightness in Rayleighs and the fluorescence efficiency (in photons s^{-1}), g, is adjusted for heliocentric Doppler shifts across the solar Fraunhofer spectrum at 309 nm (Schleicher & A'Hearn 1988). The conversion to Q_{H_2O} (Table 1) is made by dividing Q_{OH} by BR_{OH}, the branching ratio of water dissociation to OH (Table 2).

The principle advantage of aperture summation for the determination of Q_{H_2O} is that it does not require any specific knowledge of the structure of the coma, and is therefore not dependent on models of the radial distribution. Its primary disadvantage is that it provides only Q_{H_2O}, without any understanding of the other characteristics of the coma; however, when coupled with spatial imaging data, the knowledge of Q_{H_2O} can be used with radial measurements of the brightness distribution to obtain structural information about the coma.

TABLE 2
ORBIT AND SOLAR CYCLE SPECIFIC PHOTOCHEMICAL PARAMETERS OF OH PRODUCTION AND FLUORESCENCE AT 1 AU

Parameter	Value
H_2O dissociation branching ratio.....	86%[a]
Dissociation rate of H_2O.....	1.043×10^{-5} s^{-1} [b]
Dissociation rate of OH	7.491×10^{-6} s^{-1} [b]
OH fluorescence g-factor.....	4.54×10^{-5} s^{-1} [c]

[a] Huebner et al. 1992.
[b] Schleicher & A'Hearn 1988.
[c] Budzien et al. 1994.

2.2. *Outflow Velocity*

Maps of the velocity and spatial distribution of escaping OH are directly related Q_{H_2O}, solar UV radiation intensity, heliocentric velocity/distance, and collisional effects. When the FOV of a measurement is smaller than the radial extent of the OH coma, knowledge of the outflow velocity (V_{OH}) is also required to invert the OH brightness distribution to Q_{H_2O} (Cochran & Schleicher 1993), because V_{OH} and Q_{OH} are proportional in a radially expanding flow.

Variation of the OH velocity distribution with cometocentric distance R_n [$V_{OH}(R_n)$], depends on the velocity of the parent H_2O molecules, the effect of any subsequent collisions of OH with coma constituents, and the excess energy from the dissociation of H_2O, which contributes a random velocity vector with a magnitude of 1.05 km s^{-1} (Huebner et al. 1992). The spatial extent of the OH coma is defined by this velocity distribution, the dimensions of the source region, the heliocentric distance of the comet, and the solar UV intensity. In most comets the $V_{OH}(r)$, particularly in the inner coma, is not known directly, and is determined by either fitting models to the radial shape of the coma or by assuming a uniform outflow velocity with an observationally based dependence on heliocentric distance (R_h), given by

$$V_{OH} = 0.85 R_h^{-2} \quad (3)$$

(Budzien et al. 1994). Aside from the few in situ measurements (Lammerzahl et al. 1987) that serve as a basis for the above equation, wide-field, aperture-averaged measurements of the line profile of radio OH emissions (Bockelee-Morvan, Crovisier, & Gerard 1990; Colom et al. 1999) are the only direct means we have for observing V_{OH}. Radio measurements generally validate the standard relation in an average sense for comets with $Q_{H_2O} < 10^{29}$ s^{-1}, but obtain higher velocities for more active comets (Bockelee-Morvan et al. 1990). The major limitations of using radio OH line profiles for V_{OH} are that the emissions are spatially averaged and are strongly quenched in the inner coma (Schloerb 1988). The effect of quenching is to bias the extracted velocity to the outer coma, masking structure in $V_{OH}(R_n)$. This is not a concern for weaker comets with a mostly ballistic coma, but it is a serious problem in active ($Q_{H_2O} > 10^{30}$ s^{-1}) comets like Hale-Bopp, where photolytic heating (see § 2.3) acts to raise the temperature of the gas and increase the bulk outflow velocity with increasing distance from the nucleus.

Deriving $V_{OH}(r)$ from the OH radial distribution while assuming that the lifetime-related parameters are known can be done in a variety of ways, ranging from variable-width aperture photometry (Colom et al. 1999; Schleicher et al. 1998) to radial intensity profile fitting with simple spherical expansion (Festou 1981; Haser 1957) or sophisticated hydrodynamic (Crifo 1995) or Monte Carlo simulations (e.g., Hodges 1990; Combi & Smyth 1988). The extent to which these techniques produce unique results is determined by the accuracy with which Q_{H_2O} is known and the radial distance out to which the OH brightness has been measured. When distances less than the OH scale length are sampled, spherical expansion models will produce a "family" of velocity fits that are all of equal quality, but indicate different values of Q_{H_2O}. The range of acceptable velocities and hence the convergence of model fits of V_{OH} improves with the increasing radial extent of the sampled profile. The most remote parts of the profile, where $I_{OH} \rightarrow 0$, are most important to the convergence of V_{OH} (Cochran & Schleicher 1993). The addition of wide-field summations of V_{OH} (Colom et al. 1999) further constrains the model.

2.3. *The Collision Zone*

Hale-Bopp is an extreme example of a comet in which collisional acceleration acts across a spatially resolved region of the coma, affecting the interpretation of both OH radial profiles and outer coma velocity measurements. Where collisions dominate, the characteristics of the flow will be modified toward a thermalized average of *all* species (parent, daughter, ion, electron, dust, etc.) that are present. Energy input will come from daughter velocity excesses resulting from photodissociation (dominated by fast H atoms) and ionization, a process that is similar to photolytic heating in planetary upper atmospheres. We can make a crude estimate of the size of the collision zone by adopting the simple case of a spherically symmetric expanding coma, with negligible dust mass loading, and the edge defined as the point at which the time between collisions goes to infinity for a particle moving purely radially away from the nucleus. Under these assumptions, a simple formula (Whipple & Huebner 1976) for the collision zone radius (R_c) is

$$R_c = \sigma Q_{tot}/4\pi V\ , \quad (4)$$

where σ is the mean molecular cross section (in cm^2) for ballistic collisions, Q_{tot} is the total gas production rate (s^{-1}) of the comet (dominated by H_2O), and V is the mean outflow velocity (cm s^{-1}) of the background gas. In practice, this is a gross approximation. The transition from a largely thermalized distribution to completely ballistic flow is gradual, extending over distances greater than R_c, while the regions where collisions fully dominate are confined to the inner ~10% of the sphere (Combi et al. 1999). Models of the 1P/Halley velocity structure (Hodges 1990) showed that, while the flow was *largely* ballistic by 6×10^4 km from the nucleus, there was residual collisional heating out to more than 2×10^5 km. While simplistic, this assumption serves as a rough guide for local conditions in the coma.

The relevance of equation (4) depends on the amount of gas production. For weak to moderately active comets at 1 AU with $Q_{H_2O} \lesssim 10^{29}$ s^{-1}, $V_{H_2O} = 0.87$ km s^{-1} (Budzien et al. 1994), and $\sigma \sim 3 \times 10^{-15}$ cm^2, the size of the collision zone is of order 2750 km at 1 AU. This is smaller than the scale lengths of most coma species and limits the effect of collisions on the nonthermal component (dissociation excess) of the daughter species velocities. Such a collision zone will also be unresolved for most observations, which means that acceleration that occurs within it will be detectable only as an increase in the uniform bulk flow that becomes larger along with the gas production rate.

For very active comets with $Q_{H_2O} \gtrsim 10^{30}$ s^{-1}, the collision sphere will be resolvable and will begin to approach the dimensions of the scale lengths of H_2O and OH. This means that a significant fraction of all water photochemistry will occur in a collisionally thick medium. Both models (Combi et al. 1999; Combi & Smyth 1988; Hodges 1990) and observations (Bockelée-Morvan et al. 1990) show that this results in a significantly hotter coma that flows more rapidly away from the nucleus. Several estimates of Q_{H_2O} (including this work, § 3.2) obtained using different methods (Colom et al. 1999; Combi et al. 2000; Woods et al. 2000) converge to val-

ues near 10^{31} s^{-1} for Hale-Bopp at perihelion, which corresponds to $R_c > 2.75 \times 10^5$ km, assuming $V \sim 1$ km s^{-1}. This distance exceeds the scale length of water (by a factor of 3) and several other coma species (both parent and daughter) at 1 AU, and has two significant implications for the coma. First, because significant photochemistry occurs inside R_c, the photochemical excess energy of the daughter species will be thermalized back into the bulk flow. Second, due to radially (R_n) dependent energy deposition across the broad, spatially resolvable collision sphere, the bulk outflow velocity $V_{\rm av}$, $V_{\rm OH}(R_n)$, and the temperature of the gas will all vary significantly with R_n. Such a velocity gradient will be detectable in the shape and extent of the OH radial brightness distribution, $I_{\rm OH}(R_n)$.

3. OBSERVATIONS AND REDUCTION OF THE OH BRIGHTNESS AND RADIAL PROFILE

The OH observations of Hale-Bopp were taken using the Burrell Schmidt Telescope, which was operated in 1997 by the Kitt Peak National Observatory (KPNO) and Case Western Reserve University. The Burrell is a 0.9 m Schmidt Cassegrain with a UBK7 corrector that provides system sensitivity down to 305 nm. For Hale-Bopp we used the KPNO SITE 2048×2048 CCD camera covering a 78.′9 FOV. Observations of OH were obtained as part of two runs (March 24–29 and April 8) that bracketed perihelion. The Burrell FOV diameter exceeded 10^7 km for Hale-Bopp over this period, a radial extent roughly 2 orders of magnitude greater than the OH scale length in a Halley class or weaker comet. The images were taken using the OH filter of the Hale-Bopp comet library (Farnham, Schleicher, & A'Hearn 2000) in single binning mode. The observations are summarized in Table 1.

3.1. *Calibration and Correction for Atmospheric Attenuation*

The most serious calibration issue for OH imaging (Farnham et al. 2000) is the strong opacity to air-mass dependence at 309 nm, an effect that was exacerbated by the low elevation of Hale-Bopp during this period. The comet began each night at its maximum elevation, which, over our time frame, ranged the equivalent of 2–3.5 air masses (Table 1), and set within 4 hr. OH images were taken on each night, but the most useful data were obtained on 1997 March 28 and April 8, when setup, acquisition, and focus were procedurally perfect, and where OH was the immediate priority for observation. The data from April 8 are of higher quality, mainly because of the lesser air mass. There were no calibration stars in the FOV of the comet images at 309 nm, so we used a series of observations of α Aur over a similar range of elevation angles as a flux standard. The integrated signal of the star was extracted from the reduced Schmidt images and compared with the unattenuated flux of α Aur as observed with the *IUE* (using the high-dispersion, large-aperture spectrum LWP 14778, NEWSIPS processing; Holberg, Barstow, & Sion 1998). The *IUE* stellar flux was taken from the spectrum over the bandpass (309 ± 3 nm) of the Hale-Bopp OH Filter (Farnham et al. 2001) and compared directly with the image data to derive the effective telescope-atmosphere throughput as a function of air mass. The corrected extinction for the Hale-Bopp images was determined by interpolating between the stellar values to the exact air mass of the comet. From the scatter in the star data we assign a conservative $\pm 15\%$ uncertainty in the extinction-corrected comet OH intensities.

3.2. $Q_{\rm H_2O}$ *from Aperture Summation*

In the full-aperture summation extraction, the flat-fielded, bias, and dark-subtracted images were converted to a series of concentric variable-diameter apertures centered on the comet nucleus. The total flux was co-added until increasing the area of the aperture failed to increase the integrated $I_{\rm OH}$ signal and a comparison with the ring summing results (see § 3.3) indicated that the scale length had been reached. The total ADU were converted to Rayleighs, and from then to $N_{\rm OH}$ and $Q_{\rm H_2O}$ using equations (1) and (2) above.

Applying this method to the OH images and using α Aur calibration gives $Q_{\rm OH} = 7.9(\pm 1.2) \times 10^{30}$ s^{-1} on 1997 March 28 and $9.17(\pm 1.4) \times 10^{30}$ s^{-1} on April 8. With ${\rm BR_{OH}} = 0.86$ (Table 2; Huebner et al. 1992), this corresponds to $Q_{\rm H_2O} = 9.31(\pm 1.4) \times 10^{30}$ s^{-1} and $10.8(\pm 1.6) \times 10^{30}$ s^{-1} on the two dates, respectively (Table 1). These values compare favorably with other measurements of $Q_{\rm OH}$ made over the same period using a similar technique (Woods et al. 2000), $Q_{\rm H_2O}$ derived from H Lyα measurements (Combi et al. 2000), and direct IR H_2O observations made near the nucleus (Dello Russo et al. 2000). These results also serve as an anchor for the use of simulations of spherical expansion in the coma (see § 4) that fit to the OH surface brightness profile $I_{\rm OH}(R_n)$, since they depend on only two unknowns, $Q_{\rm OH}$ and $V_{\rm OH}$. As shown in equation (5), a simple spherical expansion column integration provides the brightness of OH, with an approximately linear relationship between $V_{\rm OH}$ and $Q_{\rm OH}$. Then

$$I_{\rm OH}(R_n) = \frac{g Q_{\rm OH}}{2 \times 10^6 \pi V_{\rm OH} R_n^2} \times \int_0^{\pi/2} R_n \sec^2\theta \cos^2\theta \, e^{-R_n/V_{\rm OH}\tau_{\rm OH}} \, d\theta \,, \quad (5)$$

where g is the fluorescence efficiency, R_n is the cometocentric distance (cm), $V_{\rm OH}$ is the OH radial velocity, and $\tau_{\rm OH}$ is the photochemical lifetime of OH.

3.3. *Ring Summation and the* OH *Radial Brightness Distribution*

Ring summation is a powerful method for obtaining higher S/N data in areas of an image where the flux per pixel is low. It is an area-additive technique whereby all or a portion of the data points at a specific radial distance from a set ring center are co-added. In the case of a spherically expanding comet coma, the radial profile can be used to determine the average radial outflow velocity by using a form of equation (5), and from there the production rate Q. We used a dynamic summing algorithm to obtain the $I_{\rm OH}(R_n)$ profile that operates by extracting all pixels over ranges of projected R_n and position angle, filtering for salt-and-pepper noise, and then co-adding to obtain an average brightness. The width of each ring in pixels is set to the smallest value that maintained S/N > 4, up to a maximum of 75 pixels or 1.75×10^5 km at the geocentric distance of Hale-Bopp. By stepping outward in distance from the nucleus, a radial brightness profile is obtained (Fig. 1). Full $I_{\rm OH}(R_n)$ azimuthal coma averages and subarcs of 90° and 30° in P.A. were obtained using this method. The ADU per ring averages

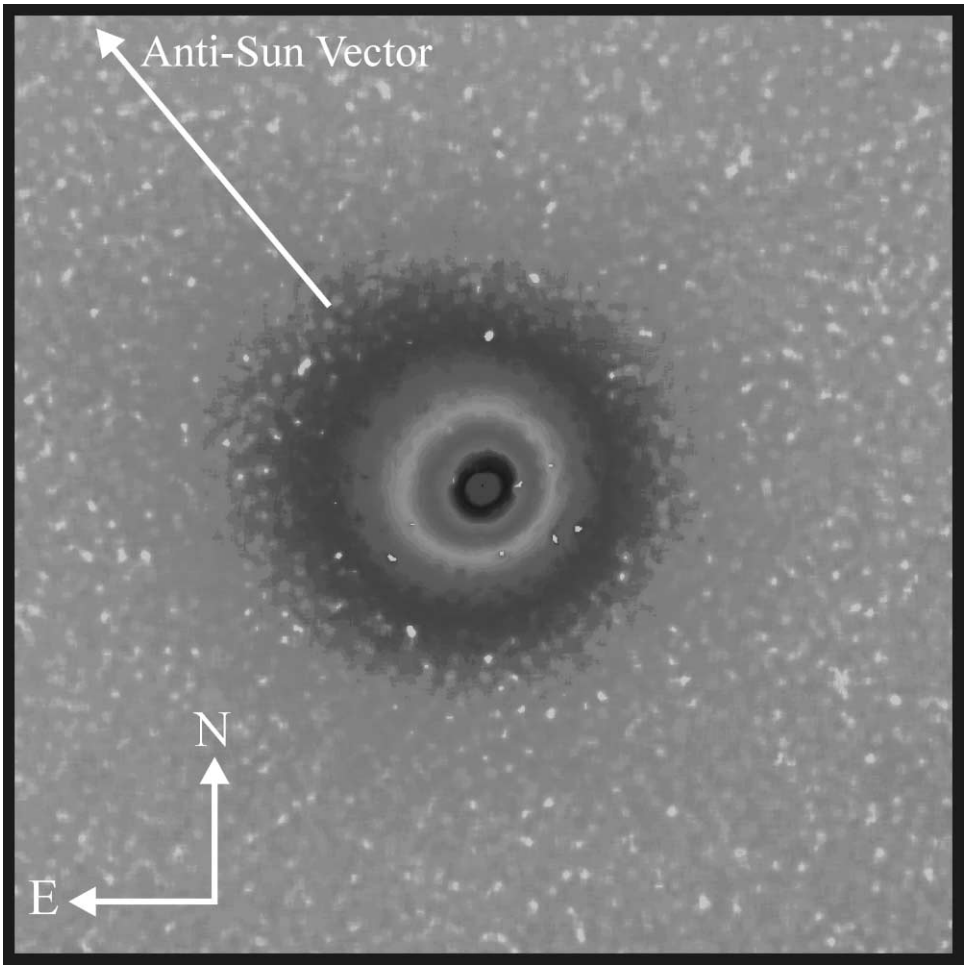

FIG. 1.—Processed OH image from 1997 April 8 showing the distribution of the emission over the total area ($\pm 10^6$ km from the nucleus) of the image extracted in a sector ring summation. The summation technique is able to detect OH emission well beyond the observable edge of the OH coma in the image by co-adding many pixels. The vector corresponding to the projected anti-Sun direction is included.

were again converted to Rayleighs based on the α Aur calibration. Ring summation of the OH coma shows that:

1. the OH coma of Hale-Bopp is more spatially extended than previously studied comets,
2. the bulk outflow velocity of the coma ($\sim V_{H_2O}$) was substantially higher than was measured from 1P/Halley at the same heliocentric distance,
3. the velocity in the coma is not uniform, but increased as a function of R_n, and
4. there is velocity structure in the coma as a function of P.A.

3.3.1. *Azimuthally Averaged Ring Summation*

The azimuthal averaged OH surface brightness radial distributions [$I_{OH}(R_n)$] show evidence of large-scale collisional acceleration across a broad expanse of the coma, from both the spatial extent of the emission and the profile gradient inside 10^4 km. Figure 2 compares the measured OH radial profile on April 8 with a simple two-component (parent and daughter) version of the Haser (Krishna Swamy 1997) model, assuming the 0.89 km s^{-1} spherical outflow derived from 1P/Halley at a heliocentric distance of 1 AU (Budzien et al. 1994; Lammerzahl et al. 1987). When the Halley class

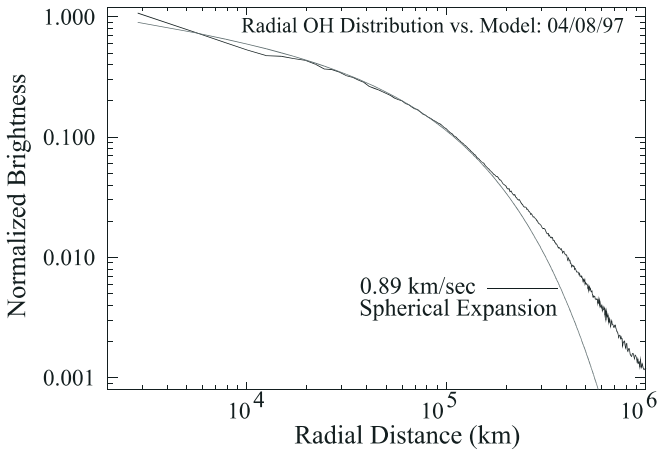

FIG. 2.—Azimuthally averaged radial surface brightness distribution of OH on 1997 April 8, compared with the best fit of a model for a uniform 0.89 km s^{-1} outflow derived from the velocity-heliocentric distance relationship of Budzien et al. (1994). The model fits the profile out to a radial distance of 2×10^5 km, but begins to fall below the data beyond this point, because of collisional acceleration in the inner coma. Production rate estimates based on this fit yield $Q_{H_2O} = 6 \times 10^{30}$ s^{-1}, which is ~30% less than those obtained from other methods (e.g., Combi et al. 2000; Colom et al. 1999).

comet model is fitted the observed profile, we obtain a close match only out a to distance of ~ 1–2×10^5 km, and derive a lower water production rate of $Q_{H_2O} \sim 6 \times 10^{30}$ s^{-1} than from aperture summation. On larger spatial scales the model fails as the simulated radial profile falls off while the observed OH distribution continues outward. Indeed, *we can find no model scenario* in which a Halley-like flow describes the outer regions of Hale-Bopp's coma or that produces a Q_{OH} equivalent to that obtained from aperture summation in the same image. We are able to use the model to simultaneously fit the outer coma and obtain a Q_{H_2O} closer to the summation value; however, this requires the assumption of a high $V_{OH} = 3.5$ km s^{-1} and produces a radial brightness profile that greatly *underestimates* I_{OH} in the inner coma. As shown in § 4, this is consistent with our general finding that a single-velocity outflow provides a poor match to the observed $I_{OH}(R_n)$ from Hale-Bopp.

3.3.2. *Ring Summation in Arcs of Position Angle*

To break down the coma and search for structure in the radial extent of the emission, we divided the coma into four 90° arcs in P.A. and obtained individual $I_{OH}(R_n)$ profiles for each. The quadrant P.A. ranges were selected so that two would be centered on the comet–Sun line, allowing a comparison of day- versus night-side gas production (Table 1). The viewing geometry toward Hale-Bopp near perihelion was particularly favorable, because the P.A.s corresponding to the orbital velocity and anti-Sun vectors were well separated. This meant that dust and ion tail vectors could also be separated into separate quadrants, which gave us four distinct coma environments (Sunward, anti-Sunward, orbit-leading, and orbit-trailing) for comparison (Fig. 3).

Close examination of the quadrants shows significant differences in the spatial extent of the emission and shape of the radial profiles consistent with a Sun–comet angle/orbital phase dependence in the velocity structure (Figs. 3*a*, 3*b*, and 4) that favors greater acceleration in the inner coma of the trailing hemisphere. Moving outward in R_n across the Sunward and orbit-leading quadrants, the I_{OH} is substantially greater in the inner ($R_n < 10^5$ km) coma than in the anti-Sun or orbit-trailing quadrants. Beyond 10^5 km the leading quadrant profiles begin to steepen and become progressively fainter relative to the trailing direction, with the $I_{OH}(R_n)$ profile in the Sunward direction always being the least spatially extended. While the magnitude of the difference in spatial extension varied between the observations, the leading/trailing profile asymmetry was a consistent feature on both dates studied, and does not appear to be related to the effects of short-term Q_{H_2O} variability. Assuming a uniform gas

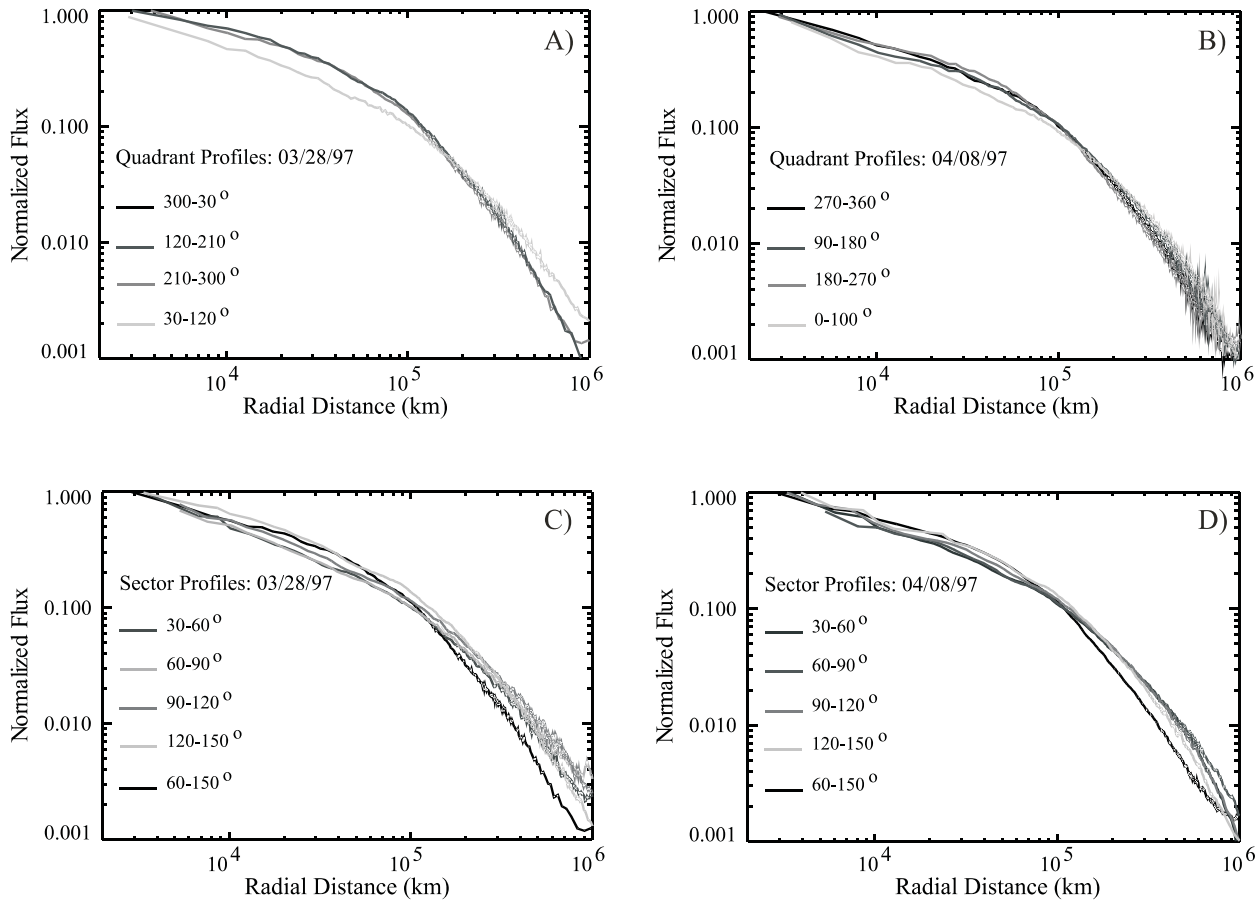

FIG. 3.—Quadrant profiles compared for each of the two nights. In (*a*) and (*b*) the four sectors covering 90° in P.A. that bracket the anti-Sun, Sunward, anti-tail, and tailward directions are compared directly. While significant differences in the degree of symmetry in the coma are obvious between the nights, there is a general trend of the anti-Sun and anti-tail profiles being shallow compared to the others inside 10^5 km and then crossing over to become more extended beyond this point. In (*c*) and (*d*), the most radially extended quadrants of the coma are broken down into 30° P.A. subsectors of position angle and then compared with the anti-tailward sector. Each subsector is considerably more radially extended that the Sunward profile, and are also responsible for most of the enhancement in the spherically averaged profile.

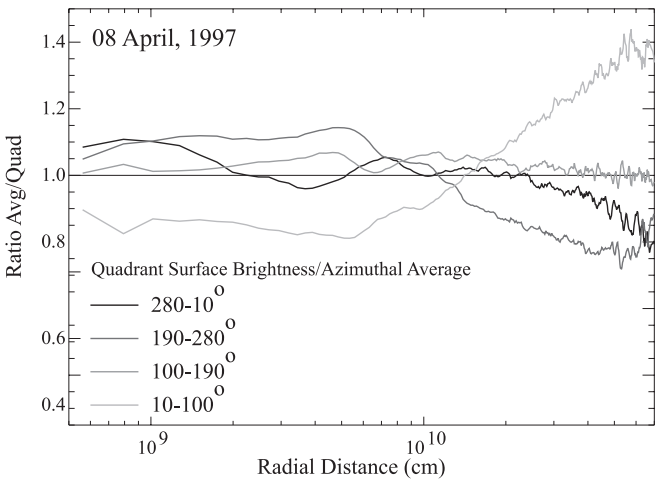

FIG. 4.—Four quadrants extracted from the data set of 1997 April 8, divided by the azimuthal average to show the differences between the quadrants. The significant departure from the average in the 10°–100° P.A. range is clearly shown. This profile is considerably shallower than average out to $\sim 10^5$ km, and then crosses over to be more extended out to the edge of the sampled field.

source distribution, the differences between the quadrant radial distributions are indicative of less acceleration occurring in the leading quadrants, causing a relative "pile-up" of molecules in the inner coma, and hence higher brightness there.

To get at the more detailed structure of the extended emission in trailing quadrants, both were further divided into three 30° subsector arcs in P.A. The shape of the $I_{OH}(R_n)$ profiles away from the nucleus in these subsectors shows that the majority of the spatial extension can be isolated to an $\sim 60°$ range of P.A. centered slightly anti-Sunward of the dust tail and extending into the region between the dust and ion tails (Figs. 3*c* and 3*d*). The enhancement itself is not tightly confined, but extends into the adjacent subsectors, eventually diminishing away from the peak back to the levels seen in the leading quadrants. The most extended subsectors appear to contribute most of the emission in the outer region of the coma both for quadrants of which they are a part, and, more significantly, *for the coma as a whole*. While the P.A. of the peak in extension does vary slightly between these dates, the basic morphology of the $I_{OH}(R_n)$ asymmetry, its general location, and its effect on adjacent subsectors does not. These characteristics are also consistent with a similar feature reported in wide-field O(^1D) images taken 3 weeks prior to our observations (Morgenthaler et al. 2001) and inner coma C(^1D) spectra taken Sunward and tailward of the nucleus on the same night (Oliversen et al. 2002).

4. COMA SIMULATION TECHNIQUES

To determine the first-order velocity structure of the coma of Hale-Bopp, we used two different forms of a simple two-component Haser model (Haser 1957; Krishna Swamy 1997). We opted for the Haser approach over the typically more accurate vectorial model (Festou 1981), because the latter assumes a daughter product velocity distribution resulting from photodissociation in the purely ballistic case, a condition that did not hold over most of the scale length of the H_2O parent in Hale-Bopp (see § 2.3). Spherical expansion models are physical idealizations of the coma that assume a constant, radial outflow that originates on the nucleus. They do not address the detailed characteristics of the coma, including extended source (icy grain) regions, azimuthal asymmetries, or temporal variations in gas production, but they nevertheless have proven useful for estimating outflow velocities and gas production rates when applied to previous comets. In addition, they have the benefit of being computationally simple, which lets us quickly sample a broad area of parameter space to fit data. Our limited aims in using such models here are to demonstrate the presence of acceleration over a significant extent of the coma of Hale-Bopp, to compare our results with more sophisticated models and other observations, and to define the range of initial and final outflow velocities and production rates that describe the observed OH distribution for use in focusing more detailed future modeling efforts.

The Haser model variations use different outflow approximations corresponding to cases of a static-velocity and an accelerating coma. In the static-velocity model, both V_{H_2O} and V_{OH} are held fixed throughout the coma, but need not be equal. In the accelerating model, we simulate collisional mixing and acceleration by forcing $V_{H_2O} = V_{OH}$ everywhere, while allowing the combined flow to increase with R_n. The other physical parameters that describe H_2O/OH photochemistry and fluorescence, including *g*-factors and lifetimes (Table 2), are set to the appropriate solar cycle, heliocentric distance, and Swings effect values found in the literature (Budzien et al. 1994; Schleicher & A'Hearn 1988) and are common to the two models. Each velocity simulation consists of three different runs of each model over spatial scales in the coma of $R_n < 10^5$ km, 10^5 km $\leq R_n < 10^6$ km, and the full profile out to 10^6 km. The output model profiles are then normalized to the data profile and evaluated by summing the point-by-point variance between the data and model. By weighting the model-data comparison higher in the inner coma and the outer edge of the radial distribution, we are able to screen out velocity combinations that fit large regions of the profile very well, but are obviously wrong at the extremes.

4.1. *The Static-Velocity Model*

The situation represented by the static-velocity model is essentially a twist on the conditions that occur in weaker comets. Acceleration in such cases occurs primarily in a small, unresolved region near the nucleus, with V_{OH} and V_{H_2O} continuing past that point as a roughly static flow. V_{OH} is roughly equal to V_{H_2O}, differing only by the spherically randomized 1.05 km s^1 excess velocity of H_2O dissociation (e.g., Festou 1981). For Hale-Bopp, we use the classical fixed velocity two-component Haser model (Krishna Swamy 1997) that produces good results for weaker comets. However, we allow for additional acceleration in the coma that takes the form of either a difference in the parent (H_2O) and daughter (OH) velocities (with restriction that $V_{OH} \geq V_{H_2O}$) or a single-velocity flow ($V_{H_2O} = V_{OH}$) that is higher than the 0.86 km s^{-1} measured for Halley. The usefulness of the static model is in revealing both the presence of acceleration and its spatial extent in the coma. If V_{OH} and V_{H_2O} are the same (i.e., $V_{OH}/V_{H_2O} = 1$), but both are larger than ~ 1 km s^{-1}, it indicates that acceleration has occurred, but was only effective in the very inner coma, in which

case the static model will produce a simulated profile that is a good approximation of the actual coma velocity structure. However, if V_{OH} and V_{H_2O} differ (i.e., $V_{OH}/V_{H_2O} > 1$), it indicates not only that acceleration has occurred, but also that it has acted over a spatially extended area of the coma. While this result identifies the presence of an extended acceleration region, the simulated radial profile is an unphysical approximation of it, because the model must treat the velocity gradient only as a difference between a fixed V_{OH} and V_{H_2O}. This tends to drive V_{H_2O} low relative to its actual value and both Q_{OH} and V_{OH} higher.

We tested the static model for a range of velocities from 0.25 to 5.0 km s^{-1} to obtain sets of $I_{OH}(R_n)$ versus V_{OH} for a given V_{H_2O} (which was also varied stepwise in velocity) in both the coma-averaged case and the four quadrants. For each V_{OH}-V_{H_2O} model pairing, the requirement that $V_{OH} \geq V_{H_2O}$ was enforced. A comparison of Q_{OH} from the model versus the aperture-summation technique was used as an external validity check, but not as a fitting criterion. The full set of model profiles were compared with the data and a grid search was performed over the entire parameter space to find the smallest data-model variance. The best model runs match the observed radial profiles closely (Fig. 5*a*), including the most spatially extended regions of the coma (Tables 3 and 4). The location of the variance minima in the parameter space of velocity and production rate converges to a narrow range varying by $\pm 10\%$ (Fig. 6), which is better than our photometric accuracy.

In Figure 6 we can see that a uniform ($V_{OH}/V_{H_2O} = 1$) outflow does not match the brightness distribution very well. The best matches for this case have variances that are more than 100 times larger than for the model minima. The smallest data-model variances are found in a pronounced minimum centered on a velocity ratio $5 < V_{OH}/V_{H_2O} < 7$, which is consistent with the second of the two cases the model is sensitive to, an acceleration process that acts over much of Hale-Bopp's coma. The velocity product in the best-case simulation ($V_{OH}V_{H_2O} = 2.7$) gives a crude estimate of the average outflow velocity over the modeled coma. We can also estimate velocity gradients implied by the model by computing the species-weighted average velocity $V_{av}(R_n)$ as a function of cometocentric distance using the equation,

$$V_{av}(R_n) = \frac{N_{OH}(R_n)V_{OH}(R_n) + N_{H_2O}(R_n)V_{H_2O}(R_n)}{N_{OH}(R_n) + N_{H_2O}(R_n)}, \quad (6)$$

where $N_{OH}(R_n)$ and $N_{H_2O}(R_n)$ are the column densities (count per cm^{-2}) of these species. This function shows a strong inner coma velocity gradient that diminishes beyond the water scale length.

The consequences of broad acceleration for the static model are found in the magnitude of V_{OH}, which is 1.5 to 2 times larger than the direct measurement of Colom et al. (1999), and Q_{OH}, which translates to a Q_{H_2O} 1.3 to 1.5 times greater than aperture summation. An indirect symptom of the model failure is the tie of Q_{H_2O} to V_{OH} (Tables 3 and 4), with the production rate increasing to compensate for the higher velocities in the more radially extended regions of the coma.

4.2. *Simulations of Variable Velocity Expansion*

Based on the apparent presence of acceleration across the bulk of Hale-Bopp's coma, an improvement in the physical accuracy of the model profiles should be achieved by adopting a single parent-daughter velocity that changes with cometocentric distance. Accelerating spherical expansion models (Hu 1990) are typically avoided, because the acceleration regions of most comets are confined to the unresolved extreme inner coma, and because the Haser approach offers no physical insight into the nature of the acceleration or how to implement it. To avoid taking an entirely ad hoc approach to this problem, we draw from the basic elements of the more detailed one-dimensional dusty-gas hybrid kinetic–Monte Carlo/dusty gas–hydrodynamic model of Hale-Bopp provided in Combi et al. (1999) as a starting point for developing a simple variable-velocity spherical expansion model. Their model has the coma effectively breaking down into two regions. Close to the nucleus, fast H atoms formed by H_2O and OH dissociation are rethermalized into the bulk flow. This heats and accelerates the coma out to a distance, defined by Q_{tot} and R_H, where H collisionally decouples from the background gas. Past this point, the primary source of acceleration shifts from the diminishing collisional component to a passive filtering of

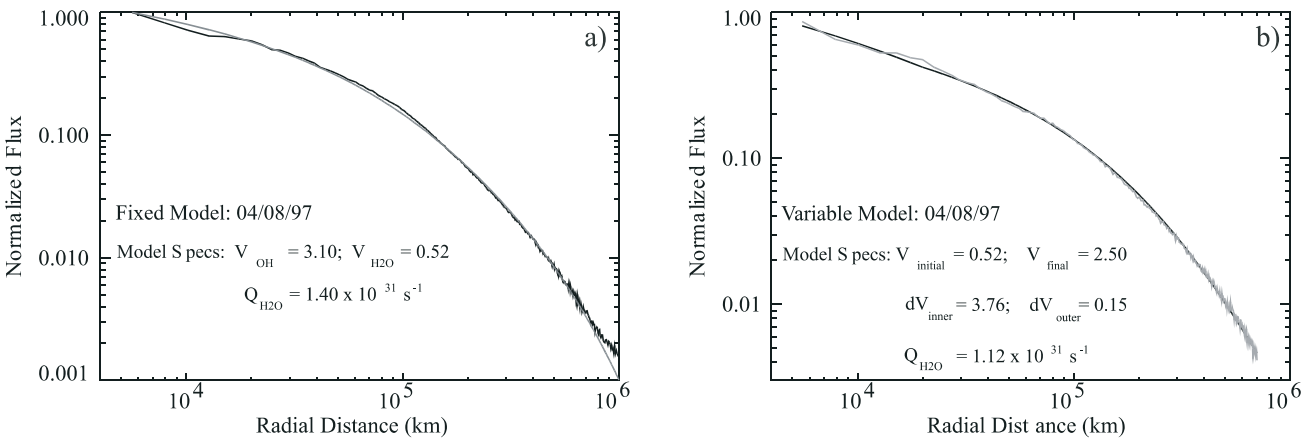

FIG. 5.—Sample model fits shown for the spherically averaged OH radial distribution on 1997 April 8, using the (*a*) fixed-velocity and (*b*) variable-velocity models. The parameters of the model outputs are shown in each case. Both models indicate the presence of acceleration over much of the coma, with the variable case providing a much closer match to Q_{H_2O} and $V_{OH}(r)$ values obtained from other measurements.

TABLE 3
RESULTS OF FIXED-VELOCITY SIMULATION FITS SHOWN AS A COMA AVERAGE AND BY QUADRANT FOR BOTH NIGHTS

P.A. Range (deg)	V_{H_2O}	V_{OH}	$Q^{31}_{H_2O}$ $(\times 10^{31}\ s^{-1})$	Sector
1997 March 28				
0–360	0.52 ± 0.07	3.25 ± 0.30	1.44 ± 0.09	Average
210–	0.56 ± 0.12	2.35 ± 0.35	1.30 ± 0.10	Anti-tail
120–	0.60 ± 0.16	2.35 ± 0.35	1.40 ± 0.09	Sunward
30–120	0.60 ± 0.08	4.65 ± 0.55	1.72 ± 0.11	Tailward
300–30	0.48 ± 0.04	3.80 ± 0.50	1.31 ± 0.12	Anti-Sun
1997 April 8				
0–360	0.53 ± 0.07	3.20 ± 0.30	1.30 ± 0.05	Coma average
270–0	0.56 ± 0.04	2.65 ± 0.25	1.19 ± 0.05	Anti-tail
180–	0.44 ± 0.16	2.60 ± 0.50	1.09 ± 0.10	Sunward
90–180	0.52 ± 0.08	2.95 ± 0.35	1.28 ± 0.06	Tailward
0–90	0.68 ± 0.08	4.00 ± 0.30	1.51 ± 0.06	Anti-Sun

the thermal distribution, where the slowest component of the OH thermalized velocity distribution is photodissociated at a greater rate at a given cometocentric distance, because its scale length, $B_{OH} = V_{OH}\tau_{OH}$, is smaller. The collisional and passive acceleration zones are approximated in our simulations with different linear velocity gradients on either side of a contact radius. At all locations in this model $V_{OH} = V_{H_2O}$, and excess formation energy is assumed to be rethermalized to the bulk gas flow. The initial velocity, velocity gradients, and the location of the contact radius are the permitted input variables.

Runs of the accelerating model across the same range of velocity space have local minima in the variance that are $\sim$10 times smaller than the static-velocity case, while Q_{OH} and outer coma V_{OH} are more in line with the aperture-summation results and other observational data. The input parameters for the best cases were for a contact radius 1–2×10^4 km, an initial velocity of $\sim$1.0 km s^{-1}, a final velocity of 2.3–2.6 km s^{-1}, and a $Q_{H_2O} \sim 0.8$–1.0×10^{31} that is equal to the aperture-summation value (Tables 3 and 4; Fig. 5*b*). The velocity gradients were much steeper inside the contact region than beyond it. These parameters all match the best available measurements of Q_{H_2O} (Combi et al. 2000), V_{H_2O} and V_{OH} (Colom et al. 1999), and the predictions of the Combi et al. (1999) dusty gas model.

When the model results are compared sector by sector in P.A., Q_{H_2O} is more uniform through the coma than in the fixed case. This is expected if the source function *is* nucleus-centered and both V_{OH} and V_{H_2O} can accelerate with R_n. We also find that the leading hemisphere is less accelerated than the trailing one, with the most spatially extended sectors being fitted by a larger outflow velocity at 10^6 km than those in the coma average. The largest velocity gradients in the coma average and trailing hemisphere are found inside the collision sphere, although most of the acceleration occurs in the outer coma, where the velocity gradient is significantly smaller, but acts over a substantially greater distance. On March 28, the leading sectors of the coma were fitted best by an acceleration profile that had no gradient inside the collision zone. Whether this is an artifact of the model or indicative of a physical mechanism such as dust-mass loading (Combi et al. 1999) is not clear from our simple treatment.

5. COMPARISONS OF THE MODEL VELOCITY DISTRIBUTION WITH OTHER DATA AND MODELS

5.1. *Radio Outflow Velocity Measurements*

As a check on the results of our models, we compared the derived velocities with the aperture-summed radio measurements of Colom et al. (1999) and Biver et al. (1999), both of whom obtained velocity and production rate data for Hale-Bopp on dates overlapping with our measurements. To obtain an areal average from the model radial velocity profiles involved computing a number-density–weighted, line-of-sight–integrated velocity at each radial distance from the nucleus out to the edge of the radio measurement FOV, weighting each ring by its ratio with the full sampled area, and then co-adding all of the rings to obtain an average outflow velocity. The main caveat to this approach is that our simple model produces line-of-sight velocities assuming pure radial expansion without vectorial or thermal dispersion in the velocity distribution. However, the trapezoid

TABLE 4
VARIABLE-VELOCITY MODEL FOR BOTH NIGHTS

P.A. Range (deg)	V_O	V_C	V_{edge}	dV_1 $(10^5\ s^{-1})$	dV_2 $(10^5\ s^{-1})$	Q_{H_2O}
1997 March 28						
0–360	0.94 ± 0.26	1.07 ± 0.07	2.64 ± 0.02	1.25 ± 1.25	0.20 ± 0.01	9.70 ± 0.55
30–120	0.88 ± 0.10	0.88 ± 0.10	1.78 ± 0.25	0.0	0.15 ± 0.06	8.95 ± 1.10
120–210.....	0.94 ± 0.10	0.94 ± 0.10	1.74 ± 0.25	0.0	0.14 ± 0.05	9.80 ± 0.77
210–300.....	1.05 ± 0.30	1.36 ± 0.15	2.10 ± 0.20	3.1 ± 2.0	0.11 ± 0.04	11.5 ± 1.1
300–30	1.02 ± 0.33	1.21 ± 0.13	2.22 ± 0.32	1.9 ± 1.5	0.14 ± 0.07	8.85 ± 0.55
1997 April 8						
0–360	0.94 ± 0.10	1.14 ± 0.22	2.52 ± 0.25	2.0 ± 1.8	0.24 ± 0.07	9.30 ± 0.60
0–90	0.90 ± 0.10	1.04 ± 0.10	2.24 ± 0.50	1.4 ± 1.3	0.21 ± 0.10	9.13 ± 0.31
90–180	0.88 ± 0.17	0.94 ± 0.12	2.50 ± 0.50	0.6 ± 0.5	0.27 ± 0.08	8.70 ± 0.59
180–270.....	1.02 ± 0.30	1.16 ± 0.16	2.65 ± 0.35	1.2 ± 1.0	0.23 ± 0.08	10.1 ± 0.9
270–360.....	1.05 ± 0.35	1.43 ± 0.20	2.70 ± 0.24	3.8 ± 3.0	0.19 ± 0.05	11.1 ± 1.0

NOTE.—Here V_{edge} is the velocity at the edge of the modeled radial profile of OH, and dV_1 and dV_2 are respectively the velocity gradients inside and outside the contact radius used in the model to break the coma into two regions.

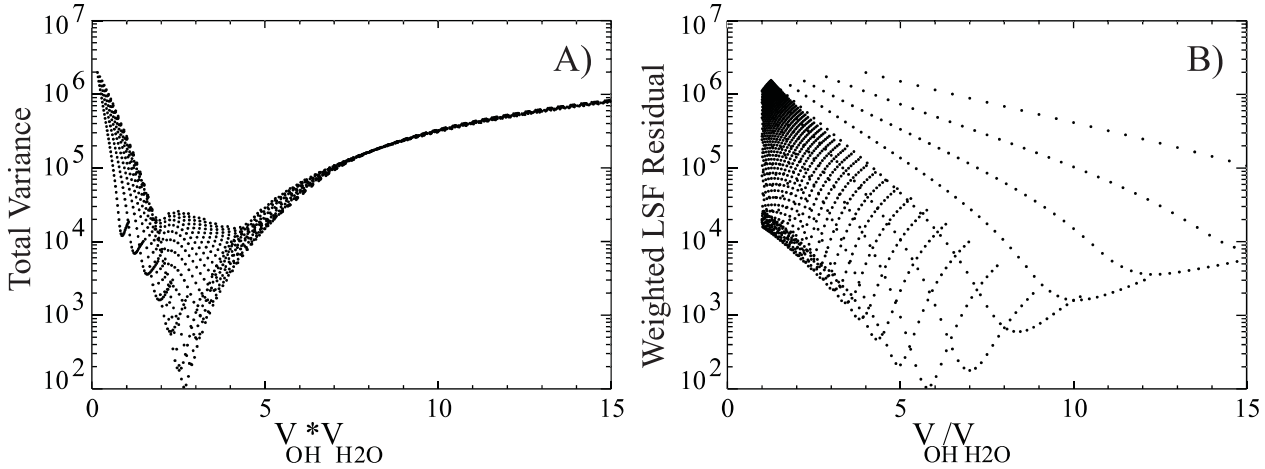

FIG. 6.—Statistics of weighted least-squares difference vs. two tests of convergence for all cases in the fixed-velocity model. (*a*) Product of the OH and H_2O velocities. The convergence onto a narrow range in the cases of close fits is consistent with the two velocities tracking each other inversely in the model. (*b*) Ratio of the velocities, revealing the degree of acceleration in the inner coma. The minimum of the distribution changes between the quadrants, with the largest values occurring for the radially extended sectors. Also evident here is the overall low quality of uniform, or close to uniform, single-velocity outflow, which is a value of 1 here. The fit indices for this case are ~2 orders of magnitude larger.

method (Bockelee-Morvan et al. 1990) used in the reduction of the radial data also isolates only the radial velocity component, which is the equivalent of our model velocities. The two methods are therefore sufficiently similar in approach to make a comparison valid.

5.2. *Inner Coma Velocities*

Biver et al. (1999) provide velocities over different regions of the inner coma, but they do not specifically measure OH. Indeed they cannot, since virtually all of it would be quenched at such small distances from the nucleus (Schloerb 1988; Schloerb et al. 1999). Instead, they use several different species, including HCN, CO, H_2S, CH_3OH, CS, and H_2CO, to derive the expansion velocity over the $1–5 \times 10^4$ km half-power width of their beam. Given the extent of the collision sphere, and clear evidence for acceleration across the inner coma, it is reasonable to assume that the outflow at any given point over this region is the same for all gas species. In the case of the inner coma of Hale-Bopp, therefore, it appears at first glance that one species is as good as another for sampling the bulk flow. However, an important factor to pay attention to is how the differences in radial distribution for the different species affect the areal-averaged velocity. Every constituent of the coma will have different radial characteristics defined by its scale length, whether it is a parent or a daughter species, or whether it has an extended source distribution. Depending on the relative brightness distributions of two species, they can have very different "area-averaged" velocities, despite being entrained in the same flow. The extent to which Biver et al. (1999) accounted for this in their measurements is unclear, but it must have been a significant effect given the spread of scale lengths for the species they measured. For our purposes, we ran a variable-velocity simulation for the set of acceleration parameters corresponding to the model run with the smallest variance, while inserting a species with a scale length equal to that of HCN (Huebner et al. 1992) and assuming a nucleus-centered source. Using Figure 2 of Biver et al., we find an HCN outflow velocity of 1.4 ± 0.1 km s^{-1} for the period surrounding perihelion, which is consistent with our derived value of $V_{HCN} = 1.2 \pm 0.15$ km s^{-1} to within their relative errors.

5.3. *Intermediate Distances*

Colom et al. (1999) directly measured the velocity of OH over a much larger area than Biver et al. (1999), using an asymmetric [3.′5 × 19′, $(2 \times 10^5) \times (1.1 \times 10^5)$ km] beam to obtain a coma-averaged outflow velocity (V_{av}). We are able to compare our model with this result, with the primary caveat that we must also address the effect of quenching in the radio measurements. Schloerb et al. (1999) computed the OH quenching radius (R_Q) for Hale-Bopp to be 5×10^5 km. Since only OH molecules at distances $\geq R_Q$ are detectable in radio observations, Colom et al. (1999) therefore measured a velocity average that was strongly biased to the outer coma. If acceleration occurs within the quenching radius, the result will be a higher radio-measured coma-averaged velocity relative to our model, which samples all regions equally. The two methods will return the same value only for the cases of zero acceleration or acceleration in a spatially small region near the nucleus. The size of the difference between our model and the radio measurement is indicative of the magnitude of the acceleration and the range of R_n over which it occurs. When our best model runs are velocity-averaged over the Colom et al. (1999) FOV, we obtain a value of $V_{av} \sim 1.7$ km s^{-1} for the full coma average, which is considerably smaller than their measured $V_{av} \sim 2.2$ km s^{-1}. This comparison can be taken as evidence of a broad acceleration or a failure in the model technique. To distinguish between these, we carry the model-data comparison further by incorporating quenching effects into the model such that we restrict the contributing OH emission to a shell surrounding the nucleus with an inner radius equal to R_Q. Averaging only the velocities in this extended region of the coma results in a model-average velocity of $V_{av} = 2.3$ km s^{-1}, which is close to the radio measurement.

5.4. *Comparison with Predictions Based on Previous Active Comets*

Very little data exists on the characteristics of comets with $Q_{H_2O} \sim 10^{31}$ s^{-1}, and most of the predictions are merely an

extension of the behavior of weaker comets to this scale. In this sense, Hale-Bopp is in a class of its own with respect to coma dynamics and provides the best opportunity to date to test the accuracy of these predictions. When $Q_{H_2O} \sim 10^{31}$ s^{-1}, the collision sphere radius exceeds the scale length of water at 1 AU, opacity effects become significant, and other processes, such as parent/daughter/granddaughter collisions, chemistry (e.g., Komitov 1989), and ion-neutral interactions, may begin to emerge. Bockelée-Morvan et al. (1990) have compiled the most extensive listing of Q_{H_2O} versus V_{H_2O} in active ($Q_{H_2O} > 10^{29}$ s^{-1}) comets, and their data show clear evidence of an upturn in the outflow velocity for active comets. Hale-Bopp is a validation that this trend continues with increasing activity, although perhaps not to the extent implied by those weaker comets. Cochran & Schleicher (1993) took the Bockelée-Morvan results a step further by fitting them to a power-law modification of the standard Q-V relationship,

$$V_{OH} = 0.85 R_h^{-2} (Q/10^{30})^{0.5} , \quad (7)$$

which, as a graphical fit, is a somewhat ad hoc result. Using their equation we can obtain a value of $V_{H_2O} \sim 3.25$ km s^1 for a comet with $Q_{H_2O} = 10^{31}$ s^{-1} and $R_h = 0.91$ AU. This value is substantially higher than what we obtain from the variable-velocity model or was observed in the aperture-average velocity (Colom et al. 1999). Interestingly, it does match the velocity required to fit the outer coma in the static-velocity case (Tables 3 and 4). What appears to differentiate Hale-Bopp from the comets that were used in the Bockelée-Morvan study is the range of R_n over which the collisional heating was effective, the relative sizes of the collision zone, and B_{OH}.

6. POTENTIAL SOURCES OF THE EXTENDED EMISSIONS

The OH enhancement in the sector between the anti-Sun and orbit-trailing directions could have one source or several mechanisms acting together to produce it. Some of these are unlikely or can be easily shown to be inadequate. For example, the magnitude of radiation pressure on OH is only enough to accelerate the gas by ~0.01 km s^{-1} over our field of view, which is far too small to be relevant to this case. We discuss here four mechanisms that could produce an apparent enhancement, including dust contamination from the tail, distributed gas production from icy grains, dust mass loading in the leading hemisphere, and an ion-neutral interaction.

6.1. *Dust Contamination*

While OH emission dominates over continuum in the regions near the nucleus, dust contamination may be significant in the outer parts of the coma, where the OH brightness is lower. If improperly accounted for, the dust scattering of the solar continuum could produce a false region of enhancement. This effect is most important where the dust is concentrated along the tail and extending back toward the anti-Sunward vector, which is also where the extended OH emission regions are observed. Mogenthaler et al. (2001) addressed this in their processing of a similar O(^1D) enhancement, and determined that the continuum was neither bright enough or distributed in a way that could cause the observed effect. To check for possible dust continuum

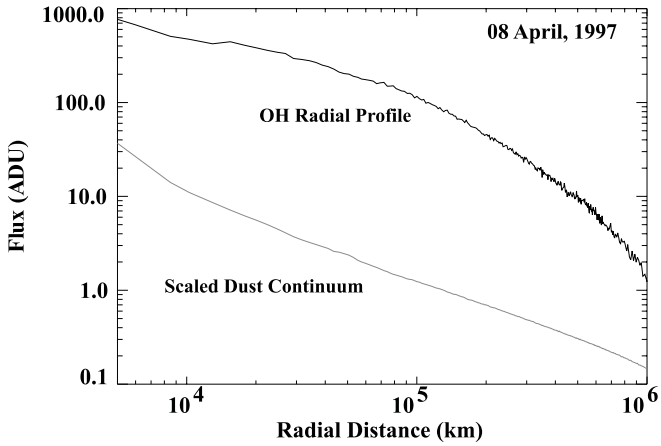

FIG. 7.—Radial profile of the most extended subsector of the OH coma, compared with the scaled residual dust continuum in the same sector. As can be seen, the contribution of the dust to the radial shape observed in the OH is not large enough to significantly affect the basic characteristic of the extension relative to the other sectors.

contamination in our data, we made a direct comparison of the radial shape and brightness of the dust and OH in the enhanced sectors, using a continuum image obtained on the same night as the April 8 OH data as a dust flux standard. The image was taken using the blue continuum (444.6 ± 3.1 nm) filter of the Hale-Bopp filter library, covering the same field of view. After correcting for instrument sensitivity, atmospheric attenuation, and the relative spectral intensity of the dust continuum at 310 nm versus 445 nm, a radial dust profile was extracted over the subsector corresponding to the greatest radial enhancement of OH. In direct comparison (Fig. 7), the dust and OH radial distributions differ on two levels that allow us to eliminate dust as the source of the trailing extension. First, the shape of the dust profile is significantly shallower with radial distance than that of OH. Second, its brightness contribution is only ~2%–10% that of OH out to distances greater than 10^6 km.

6.2. *Icy Grain or Debris Evaporation*

While we can demonstrate that scattered solar continuum from dust does not contribute significantly to the OH radial distribution, the dust lane does cover areas of the enhanced regions and could thus still affect the OH radial distribution through outgassing from grains and larger debris in the tail. It is not possible to completely exclude this process as a contributor, but it would have several effects on coma structure that make it an unlikely source of the increased spatial extent of OH. The distribution of evaporative grains would need to be approximately uniform throughout the tail sectors to produce the smooth radial shape seen in the OH data. The source of evaporating grains would have to have been continuous over a period of more than a month to account for the persistence of the feature in OH, O(^1D) and C(^1D) images and spectra (Morgenthaler et al. 2001; Oliversen et al. 2002). Finally, any OH produced beyond 2×10^5 km would be in the ballistic coma, and thus not accelerated beyond the addition of the grain motion and the 1.05 km s^{-1} excess formation velocity of OH from H_2O. Because the distribution of OH is dominated by the extended sectors beyond 5×10^5 km, such a velocity admixture would be reflected in the aperture-summation measure-

ments of Colom et al. (1999) as a reduced V_{av} that is not observed.

6.3. *Dust Mass Loading*

Several studies of the Hale-Bopp coma have concluded that dust grain production was largely confined to the sunlit hemisphere of the nucleus (Rauer et al. 1997; Weaver et al. 1997), while gas production was more uniformly distributed (Samarasinha, Mueller, & Belton 1999). In the inner coma regions, where photolytic heating was most effective in accelerating the neutrals, collisions with the local dust grain population would absorb a portion of the thermal energy and impede the acceleration and heating of the gas, at least near the nucleus. The spatial extent and efficiency of the dust-loading process in Hale-Bopp was examined by Combi et al. (1999), who looked at the effect on outflow for different cases of an active sector on the nucleus with various dust grain size distributions. While the magnitude of the interaction is highly dependent on unknown elements of the dust grain size, Combi et al. (1999) does show significant mass loading of the flow in the dusty areas. This could explain certain aspects of the spatial structure seen in OH, particularly the fact that the Sunward quadrant was consistently less extended than the others. However, the magnitude of the effect in the Combi et al. model is significantly less than is observed between the leading and trailing hemispheres in OH. Moreover, this process fails to predict a focused acceleration in the dust-free zone, but rather produces focused deceleration in the Sunward direction.

6.4. *Ion-Neutral Coupling*

Photoionization and solar wind mass loading provide a considerable source of energy input to the trailing hemisphere of the coma that could be tapped to produce a vectored acceleration in the neutral component in a manner similar to that observed in planetary ionospheres. Newly formed ions in the inner coma will be picked up by the magnetized solar wind and accelerated in the solar wind flow direction at a rate that depends on the density, velocity, and field strength in the local wind. The slower comet ions will mass load the solar wind, but, depending on the coma gas density, may in turn be mass loaded by interactions with inner coma neutrals, which are moving both radially away from the nucleus and in the direction of the comet orbit. This latter (orbital) component is largest at perihelion and acts perpendicular to the solar wind acceleration. In a high-density coma, ions may have several interactions with neutrals before escaping the ballistic regime that will both retard their acceleration and deflect them in the orbit direction. Hale-Bopp's large Q_{H_2O} provided a substantial source of coma gas density; however, the strength of any ion-neutral coupling would also depend on the solar wind characteristics and the different charged-particle scattering cross sections of the molecular species. Limited observational support for such an interaction is found in observations of inner coma ion distribution and densities made by Anderson (1999). These data show smooth acceleration of H_2O^+ at 0.161 m s^{-2} on 1997 March 16, and 0.197 m s^{-2} on 1997 April 21, out to more than 2×10^6 km from the nucleus. This acceleration is 3–10 times smaller than was derived for Halley in 1986 (Scherb et al. 1990). Anderson (1999) attributes this retardation to solar wind mass loading by the substantial population of comet ions. Since both solar wind and ion/neutral mass loading produce the same observed effect in the Anderson data, it is not possible to distinguish between the two processes based solely on the available data, at least not without either direct measurements of the solar wind (which were not made for Hale-Bopp) or detailed modeling of interaction that is beyond the scope of this work.

7. SUMMARY

We have derived Q_{H_2O} from wide FOV images of OH emission from Hale-Bopp using aperture summation and $V_{OH}(r)$ from static- and variable-velocity spherical expansion models that assume an unresolved H_2O source region. The resulting integrated OH brightness and Q_{H_2O} are consistent with other observations taken near perihelion, while model fits to the radial distribution of OH show a significant enhancement in the cometocentric extent of the emission relative to weaker comets. Static-velocity spherical expansion modeling indicates strongly that acceleration occurred over a substantial region of the coma. This conclusion is reinforced with the somewhat more physically realistic variable-velocity simulations, which suggest increasing outflow velocity with increasing R_n that is characterized by a steep velocity gradient inside a collision zone and a broad region of slower acceleration over the rest of the coma. These results are consistent with the extrapolated predictions of coma structure for very active comets that are based on a combination of models (Combi & Smyth 1988) and observations (Bockelee-Morvan et al. 1990; Schleicher et al. 1998). When compared to published radio measurements of V_{OH} and Q_{H_2O} (Biver et al. 1999; Colom et al. 1999), our models match coma averages over fields of 10^4 km and 2×10^5 km.

When the coma is broken down into quadrants, a significant asymmetry in the OH radial distribution emerges in the shape of the profiles on all scales within the coma. The OH brightness distributions in the trailing hemisphere are generally shallow compared to the leading hemisphere in the inner coma, but cross over at intermediate distances to become brighter and more spatially extended. This behavior was a common characteristic of each observation and is similar to an azimuthal asymmetry observed in O(^1D) (Morgenthaler et al. 2001) and C(^1D) (Oliversen et al. 2002). Detailed study of the spatial extension shows it to be primarily focused into a 60° range of P.A. between the dust tail and the anti-Sunward direction. Model fits for these regions suggest that greater acceleration occurred in these regions than elsewhere in the coma. We have discussed several possible sources for the enhancement, including a wider trailing hemispheric collision region, icy grain outgassing in the dust tail, reduced dust mass loading in the trailing hemisphere, and a vectored ion-neutral interaction with the solar wind and comet ions. Additional modeling is required to distinguish among those processes that cannot be discounted as a contributing factor.

REFERENCES

Anderson, C. M. 1999, Earth Moon Planets, 78, 99
Biver, N., et al. 1999, Earth Moon Planets, 78, 5
Bockelée-Morvan, D., Crovisier, J., & Gerard, E. 1990, A&A, 238, 382
Budzien, S. A., Festou, M. C., & Feldman, P. D. 1994, Icarus, 107, 164
Cochran, A. L., & Schleicher, D. G. 1993, Icarus, 105, 235
Colom, P., Gerard, E., Crovisier, J., Bockelée-Morvan, D., Biver, N., & Rauer, H. 1999, Earth Moon Planets, 78, 37
Combi, M. R., Kabin, K., DeZeeuw, D. L., Gombosi, T. I., & Powell, K. G. 1999, Earth Moon Planets, 79, 275
Combi, M. R., Reinard, A. A., Bertaux, J.-L., Quemerais, E., & Mäkinen, T. 2000, Icarus, 144, 191
Combi, M. R., & Smyth, W. H. 1988, ApJ, 327, 1026
Crifo, J. F. 1995, ApJ, 445, 470
Dello Russo, N., Mumma, M. J., DiSanti, M. A., Magee-Sauer, K., Novak, R., & Rettig, T. W. 2000, Icarus, 143, 324
Farnham, T. L., Schleicher, D. G., & A'Hearn, M. F. 2000, Icarus, 147, 180
Festou, M. C. 1981, A&A, 95, 69
Haser, L. 1957, Bull. Soc. R. Sci. Liége, 43, 740
Hodges, R. R. 1990, Icarus, 83, 410
Holberg, J. B., Barstow, M. A. & Sion, E. M. 1998, ApJS, 119, 207
Hu, H.-Y. 1990, Ph.D. thesis, Univ. Arizona
Huebner, W. F., Keady, J. J., & Lyon, S. P. 1992, Ap&SS, 195, 7
Komitov, B. 1989, Adv. Space Res., 9, 177
Krishna Swamy, K. S. 1997, Physics of Comets (2d Ed.; Singapore: World Scientific)
Lammerzahl, P., et al. 1987, A&A, 187, 169
Morgenthaler, J. P., Harris, W. M., Scherb, F., Anderson, C. M., Oliversen, R. J., Doane, N. E., Combi, M. R., Marconi, M. L., & Smyth, W. H. 2001, ApJ, 563, 451
Oliversen, R. J., Doane, N. E., Scherb, F., Harris, W. M., & Morgenthaler, J. P. 2002, ApJ, in press
Rauer, H., et al. 1997, Science, 275, 1909
Samarasinha, N. H., Mueller, B. E. A., & Belton, M. J. S. 1999, Earth Moon Planets, 77, 189
Scherb, F., Magee-Sauer, K., Roesler, F. L., & Harlander, J. 1990, Icarus, 86, 172
Schleicher, D. G., & A'Hearn, M. F. 1988, ApJ, 331, 1058
Schleicher, D. G., Millis, R. L., & Birch, P. V. 1998, Icarus, 132, 397
Schloerb, F. P. 1988, ApJ, 332, 524
Schloerb, F. P., Devries, C. H., Lovell, A. J., Irvine, W. M., Senay, M., & Wootten, H. A. 1999, Earth Moon Planets, 78, 45
Schultz, D., Li, G. S. H., Scherb, F., & Roesler, F. L. 1993, Icarus, 101, 95
Smyth, W. H., Marconi, M. L., Scherb, F., & Roesler, F. L. 1993, ApJ, 413, 756
Van Dishoeck, E. F., & Dalgarno, A. 1984, Icarus, 59, 305
Weaver, H. A., et al. 1997, Science, 275, 1900
Whipple, F. L., & Huebner, W. F. 1976, ARA&A, 14, 143
Woods, T. N., Feldman, P. D., & Rottman, G. J. 2000, Icarus, 144, 182